Research Paper

Photoelectrodeposition of Pt nanoparticles on Sb_2Se_3 photocathodes for enhanced water splitting

Marcos Vinicius de Lima Tinoco[1], Magno Barcelos Costa[1], Lucia Helena Mascaro, Juliana Ferreira de Brito[*]

Department of Chemistry, Federal University of São Carlos, Washington Luiz Road, km 235, São Carlos, SP 13565-905, Brazil

A B S T R A C T

One of the biggest challenges around photochemical materials is to develop highly active and stable catalysts, if possible, with a simple synthesis methodology. This study presents the photoactivity of Sb_2Se_3 semiconductor containing Pt nanoparticles obtained with a fast deposition rate. The deposition of Pt nanoparticles using the electrodeposition (ED) and photoelectrodeposition (PED) methods was investigated. Even with the same electrodeposition charge, the photocatalyst prepared using PED resulted in a material with photocurrent density almost three times higher than the one prepared through ED. There is a difference in the nucleation and growth kinetics of Pt nanoparticles between the two methods. The Pt growth using ED was characterized by the agglomeration of Pt with consequent formation of larger metal particles, while PED generated new sites for the metal deposition, allowing a better distribution of Pt on the surface of the semiconductor and improving the photocurrent density, charge transfer, and photoconversion of the photocatalyst.

© 2021 Elsevier Ltd. All rights reserved.

1. Introduction

The aggravation of the shortage of energy resources from oil in the last decades has been considerably fomenting the search for high-quality alternative sources of energy [1]. The conversion of energy from solar light is a mid-term solution to the urgency in decreasing emissions of carbon dioxide (CO_2) and it can accelerate the introduction of renewable energy [2]. For that, it is essential to develop an efficient catalyst that can be applied in the conversion and storage of energy from solar light. This can be done through careful engineering of the charge transfer process, for example, optimizing the alignment of the potentials corresponding to the valence and conduction bands of the semiconductor ato coincide with the redox potential of the reaction of interest [3].

Many strategies are used to improve the photoelectrochemical activity of the semiconductor, such as doping by inserting metal species into its structure, which creates donor/acceptor impurity levels within the bandgap [4], formation of heterostructures with a buffer layer [5], the use of a favorable crystallographic orientation [6], formation of a bilayer nanostructure [7], morphology control [8], etc. Another option is to modify the material by decorating

the surface of the semiconductor with metal species, which act as photoinduced electron trappers, promoting effective charge separation [9]. In that sense, the use of photoelectrochemical methods to deposit noble metals led to small islands of cocatalysts on the surface of p-type semiconductors, improving the conversion of solar energy [10]. The light-assisted electrodeposition (photoelectrodeposition, PED) method has been widely studied [11–13]. The literature contains several studies concerning the application of PED to obtain co-catalytic systems, such as Pt deposition on InSe lamellar semiconductor [10]; Pt on p-Si semiconductor [14]; cobalt-phosphate catalysts on hematite [15]; heavy metals on SeO_x/CeO_2 photocatalysts [16], among others. The effects of the electrodeposition of metals assisted by light include activation of surface diffusion, growth of high-crystallinity films with reduced defects, the prevalence of the nucleation process, uniform distribution of the species, and the possibility to control the size and distribution of the metal nanoparticles [14,15,17,18].

Pt nanoparticles are cocatalysts largely used to improve the photoactivity of semiconductors [19–22]; Pt is the most efficient option for the H_2 evolution reaction (HER) in acidic or neutral medium [8,23,24] and it can complement well the properties of Sb_2Se_3 [25]. This semiconductor has a bandgap between 1.0 and 1.2 eV [26], a high light absorption coefficient ($>10^5$ cm^{-1}) [27], a unique crystalline phase [28], and an appropriate positioning of the CB and VB for the HER [29]. However, Sb_2Se_3 catalysts suffer

from photocorrosion in an aqueous medium and promote an elevated recombination rate of the charge carriers, which prevents a good efficiency for the HER [30]. The use of cocatalysts can minimize the photocorrosion, improve the charge transfer, and even decrease the overpotential necessary to increase the reaction rate [4,31].

The electrodeposition method (ED) is the most common method to synthesize Pt nanoparticle cocatalysts, with restriction to a potentiostatic or galvanostatic deposition using H_2PtCl_6 as a precursor [32–34]. However, different pathways can be investigated to optimize the time and cost of this deposition. In that sense, the present study aims to investigate the electrochemical and photoelectrochemical methods for the deposition of Pt nanoparticles on Sb_2Se_3 thin films and to evaluate the difference in the photoactivity of the Sb_2Se_3/Pt catalysts obtained in each case. Additionally, this research aims to optimize the time of Pt deposition seeking a high photocurrent response for the semiconductor/cocatalyst developed.

2. Experimental part

2.1. Synthesis of Sb_2Se_3 thin films

Fluorine-doped tin oxide glass (FTO, Sigma-Aldrich, ca. 1 cm x 1.5 cm) was used as a substrate for the synthesis of the Sb_2Se_3 thin film. The substrate was cleaned by ultrasonication in deionized water, ethanol, acetone, and isopropanol for 5 min in each solvent . Subsequently, the clean FTO was treated with N_2 plasma (Plasma Cleaner Zhengzhou CY-P2L-B) for 1 min using 80 W_{RF} of power and 500 mL min^{-1} of N_2 flow. To reach this condition, static contact angle measurements (goniometer Ramé-hart 260 F4) were performed on the FTO, by the sessile drop method, with and without previous cleaning with solvent and plasma (the results are in Fig. S1a). After cleaning, the Sb_2Se_3 films were electrodeposited, using a potentiostat/galvanostat (Autolab PGSTAT 302N), in a conventional three-electrode cell with FTO (exposed area of ~0.5 cm^2) as the working electrode (WE) and a Pt plate as the counter electrode (CE). The Ag/AgCl/Cl$^-$$_{(sat. KCl)}$ reference electrode (RE) was used in all experiments and, therefore, all potentials in this work were based on this reference. The elements were co-electrodeposited under −0.6 V vs Ag/AgCl/Cl$^-$$_{(sat. KCl)}$, employing a charge of 600 mC cm^{-2}, using 2.0 mmol L^{-1} SeO_2 (Alfa Aesar, >99.4%) and 1.25 mmol L^{-1} $C_8H_4K_2O_{12}Sb_2 \bullet xH_2O$ (Sigma-Aldrich, >99%) as precursors in 0.5 mol L^{-1} Na_2SO_4 supporting electrolyte (Sigma-Aldrich, > 99.9%) adjusted to pH 2 with H_2SO_4. The solution was pre-deaerated with N_2 flow for 15 min before the electrodeposition. After the deposition, the samples were thermally treated in a glass cylinder with a selenium atmosphere at 300°C for 60 min [35].

2.2. Pt deposition

For the Pt deposition, a solution of 1.0 mmol L^{-1} of $H_2PtCl_6 \bullet xH_2O$ (Sigma-Aldrich, ≥ 99.9%) was used in 0.1 mol L^{-1} phosphate buffer/0.5 mol L^{-1} Na_2SO_4 – pH 6.5 (Sigma-Aldrich, ≥ 99.0%) previously deaerated for 15 min with N_2 flow. The Pt deposition was performed using a three-electrode photoelectrochemical cell with a quartz window. The CE and the RE were the same ones mentioned above. Pt was deposited in the potentiostatic regime following two different procedures to obtain: electrodeposited Pt (ED), applying a potential of −0.1 V vs. Ag/AgCl/Cl$^-$$_{(sat. KCl)}$ for 10 min [33], and photoelectrodeposited Pt (PED) under the same conditions and assisted by light [34]. All the experiments involving illumination employed a solar simulator with a 100 W Xe lamp and an AM 1.5G filter (Oriel, LSC-100) applying a power density of 100 mW cm^{-2}

over the whole spectrum (1 sun, calibrated with a power and energy meter, Thorlabs). The solar simulator spectrum and its chromaticity diagram are shown in Fig. S1b.

2.3. Physical characterization

The electrodes were characterized concerning the structural composition using X-ray diffraction analysis (XRD, Rigaku DMax2500PC, CuKα radiation) with a scan rate of 0.2 ° min^{-1} in a 2θ range between 10 and 80°. Peak indexing was performed using the Crystallographica Search Match software. The chemical composition was investigated by Raman spectra, which were obtained under 532 nm of excitation using a modular confocal Raman microscope (Horiba). Morphological characterization was performed by scanning electron microscopy (SEM) operating with 5 kV and in-Lens detector (FE-SEM, Zeiss Supra 35). The mapping of the elements was verified using energy-dispersive X-ray spectroscopy (EDX, Philips-XL30-FEG). The optical characterization of the films was based on ultraviolet-visible-near infrared spectroscopy (UV-vis-NIR) (Cary 5E spectrometer) using an integration sphere for diffuse reflectance. The absorption coefficient, α, was determined using the Kubelka-Munk equation, while the optical energy of the bandgap, E_g, was obtained from the Tauc plot [36].

2.4. (Photo)Electrochemical characterization

The photocurrent vs. potential measurements were performed employing linear voltammetry with a scan rate of 5 mV s^{-1} and pulses of 3 s, (optical shutter, Thorlabs, SHB1) from the open circuit potential up to a potential 200 mV more negative than the thermodynamic potential of proton reduction. In total, three replicates of each sample were made so that the averages of the photocurrent values could be extracted with their respective standard deviations. Chronoamperometry was used in this system to ascertain the behavior of the films by applying a constant potential for 660 s, alternating with pulses of 60 s in the light and dark. To compare the photocurrents, the conversion of the potential vs Ag/AgCl/Cl$^-$$_{(sat. KCl)}$ to the RHE scale was done using the equation [37]:

$$E \text{ (vs RHE)} = E_{appl} \left(\text{vs Ag/AgCl/Cl}^-_{(sat. KCl)} \right)$$
$$+ \text{pH} \times 0.059 \text{ V} + 0.197 \text{ V} \qquad (1)$$

The electrode/solution interface was evaluated by electrochemical impedance spectroscopy (EIS). The experiments were carried out under constant illumination with frequencies from 0.1 Hz to 100 kHz, 0 V_{RHE}, applying a sinusoidal excitation signal of 0.01 V_{rms}. All photoelectrochemical experiments were carried out in a neutral medium, using 0.1 mol L^{-1} phosphate buffer/0.5 mol L^{-1} Na_2SO_4 – pH 6.5 (Synth). Before any experiment, each solution was previously deaerated with N_2 flow for 15 min.

3. Results and discussions

3.1. Characterization of Sb_2Se_3/Pt(ED) and Sb_2Se_3/Pt(PED)

3.1.1. Physical characterization of the catalysts

Typically, Sb_2Se_3 obtained by potentiostatic ED in the Na_2SO_4 electrolyte has the form of globular clusters of different sizes, as reported previously [38]. This can be confirmed by the SEM images of the surface of the Sb_2Se_3 film in the absence of Pt presented in Fig. 1a. After the ED of Pt (Sb_2Se_3/Pt(ED), Fig. 1(b), small particles of ~100 nm appear on the Sb_2Se_3 clusters; possibly, these nanoparticles are related to the growth of Pt on the absorber. However, the same deposition conditions in the presence of light (Sb_2Se_3/Pt(PED)), Fig. 1(c) result in a substantial coverage of Sb_2Se_3 by the Pt nanoparticles. This means that the deposition
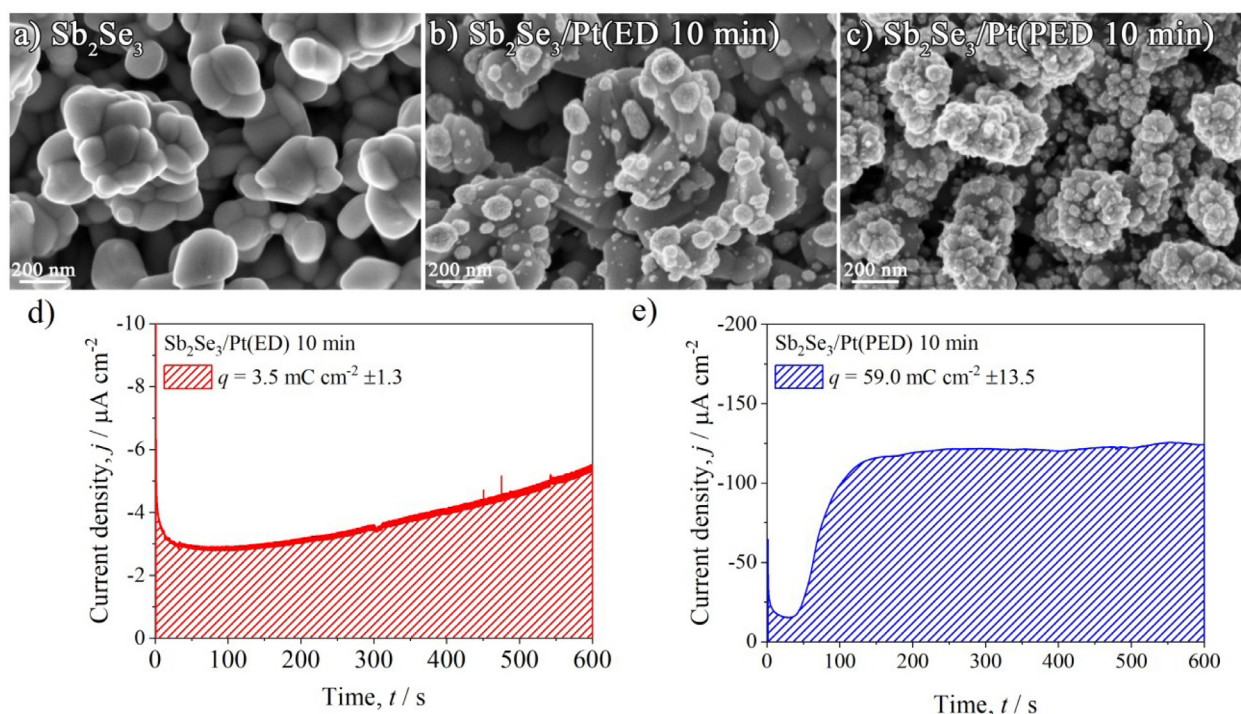
**Fig. 1.** FEG-SEM micrographs with 150k of magnification for the (a) Sb_2Se_3, (b) Sb_2Se_3/Pt(ED), and (c) Sb_2Se_3/Pt(PED) films. Deposition profiles of Pt on Sb_2Se_3 obtained during 10 min of (d) ED and (e) PED.

of Pt had its kinetics altered when the films of Sb_2Se_3 were illuminated. Even with different amounts of dispersion, the growth of the Pt nanoparticles is uniform through both methods, hence, the aforementioned characteristics are observed over the entire length of the films, as shown in Fig. S2a to S2c.

For comparison, Fig. 1d and 1e show the deposition profile of Pt with the mean values of the deposition charge for 10 min calculated by integrating each curve. A value of 3.5 mC cm^{-2} ±1.3 was obtained for Sb_2Se_3/Pt(ED), while 59.0 mC cm^{-2} ±13.5 was found for the film Sb_2Se_3/Pt(PED), a charge ~16-fold higher. This phenomenon can be associated with the photogeneration of electrons that populate the CB and create new sites on the Sb_2Se_3 surface. Some of these sites correspond to defects generated in the presence of light, which provide a more efficient separation of e$^-$/h$^+$ pairs [39]. Consequently, the photogeneration of electrons occurs preferentially in those regions, increasing the availability of sites to deposit the Pt species (additional details will be shown ahead) [13,40]. Considering that Pt species in solution can be deposited according to reactions 2 and 3, the average quantities of 1.8 and 29.7 μg cm^{-2} of metal were obtained for the films Sb_2Se_3/Pt(ED) and Sb_2Se_3/Pt(PED), respectively (calculated from Faraday's equation considering faradaic efficiency of 100%). The polarization experiments used to electrodeposit Pt were repeated in the absence of the $[PtCl_6]^{2-}$ ion in the solution, resulting in the charges of ~0.03 and 0.18 μC cm^{-2} for Sb_2Se_3/(ED) and Sb_2Se_3/(PED), respectively; these samples were treated as blanks (Fig. S2d and S2e, respectively).

$$[PtCl_6]^{2-} + 2e^- \rightleftharpoons [PtCl_4]^{2-} + 2Cl^- \tag{2}$$

$$[PtCl_4]^{2-} + 2e^- \rightleftharpoons Pt + 4Cl^- \tag{3}$$
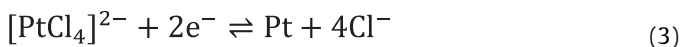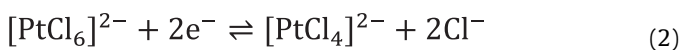
It is also interesting to point the differences in the time dependence of the current density for both deposition processes. The first part of the curve is related to the nucleation and surface diffusion of Pt atoms [41]. In the presence of light, there is an increase

in the concentration of free electrons and more sites can be photoactivated on the absorber; therefore, more nuclei are formed per unit area. The increase in the number of nuclei facilitates the deposition of Pt and the growth of the nanoparticles. So, PED results in an earlier saturation of the current density to achieve the maximal value, indicating that a steady state was achieved faster and with a higher current density compared to the procedure without illumination. According to Pastorek and coworkers [42], the decrease in the stability of the formation of the deposit can be observed by the insufficient or missing current density saturation phase in the last part of the electrodeposition curve, as can be observed in Fig. 1d.

The presence of Pt in the Sb2Se3/Pt films was investigated by EDS (Fig. S3). The results showed 0.2 and 2.1 % atomic (Pt) for Sb2Se3/Pt(ED) and Sb2Se3/Pt(PED), respectively. This almost 11-fold increase indicates a greater expression of the deposition for PED compared to ED during the same time of synthesis. The crystalline phase of Sb_2Se_3 was determined by XRD, Fig. S4a. According to the orthorhombic standard of Sb_2Se_3 (antimonselite, JCPDF 89-821) and the FTO substrate (cassiterite, JCPDF 41-1445), all peaks in the sample were indexed without the presence of any secondary phase, showing the efficiency of the method to obtain crystalline films. However, the presence of Pt cannot be confirmed by XRD, due to the lack of sensitivity of the equipment to the low quantity deposited of the metal.

The presence of Pt was also confirmed by Raman spectroscopy, which presented the main vibrational modes of the Sb_2Se_3 films and Pt on the films modified using the different deposition methods (Fig. S4b). The Sb_2Se_3 film presents an intense peak at 191 cm^{-1} and shoulders at 120 and 210 cm^{-1}, which correspond to the vibrational modes of the orthorhombic structure of the material [43]. For the Sb_2Se_3/Pt(ED) and Sb_2Se_3/Pt(PED) films, two dominant peaks emerged at 171 and 204 cm^{-1}. The appearance of these peaks may be related to Pt clusters present on the surface of the films, as seen in Fig. 1b,c. The peak at 171 cm^{-1} corresponds to the antisymmetric stretching mode of the Pt atoms, while the peak at 204 cm^{-1} corresponds to the symmetric stretching mode [44]. The peaks with lower intensities (254 and 450 cm^{-1}) correspond to the

vibrational modes of Sb_2O_3 that arise as a result of the oxidation of Sb_2Se_3 by the equipment's incident beam [43,45].

3.1.2. (Photo)Electrochemical characterization of the catalysts

The plots for the reflectance ($R\%$) and α, as well as the E_g values of the Sb_2Se_3, $Sb_2Se_3/Pt(ED)$, and $Sb_2Se_3/Pt(PED)$ films, can be seen in Fig. S5. The reflectance plot, Fig. S5a, shows that all films have values between 5 and 10 $R\%$ at wavelengths (λ) < 975 nm. However, there is a ~15% reduction in reflectance for Pt-modified films in the near-infrared region. This may be indicative of some absorption phenomenon that may occur in less energetic regions when there is Pt present on the surface of the films. The same occurs with the α of each film in the inset of Fig. S5a; in regions of near-infrared wavelengths, there is a greater interaction of the electromagnetic radiation with the material, allowing little of the incident light to be reflected. This is due to the electron longitudinal surface plasmon resonance phenomenon and is directly linked to the amount of Pt deposited [33,46]. Fig. S5b shows the Tauc plot with the extrapolation of the curve next to its baseline to obtain E_g. The presence of Pt clusters on the Sb_2Se_3 films did not change the magnitude of the E_g, since they are metallic clusters distributed regularly over the absorber. As expected, the average value of E_g was 1.20 ± 0.01 eV, following results seen in the literature [47,48]. Again, the effect of absorption in less energetic regions can be seen for the $Sb_2Se_3/Pt(ED)$ and $Sb_2Se_3/Pt(PED)$ films.

The photoelectrochemical measurements were performed by linear sweep voltammetry (LSV) under pulsed light irradiation, Fig. 2a. Moreover, an average value of the photocurrent obtained at 0 V_{RHE} from the replicates for each as-prepared material is presented in Fig. 2b. The deposition of Pt by ED and PED, on the surface of Sb_2Se_3 films, improved the photocurrent density (Fig. 2a, red and blue curves, respectively), reaching values of -0.4 ± 0.3 mA cm^{-2} and -1.4 ± 0.3 mA cm^{-2}, respectively, compared to the photocurrent of -0.10 ± 0.06 mA cm^{-2} observed for the bare Sb_2Se_3 film (Fig. 2a, black curve). This behavior is summarized in Fig. 2b. To compare the onset potentials of both films (Fig. S6), a linear extrapolation of the rising photocurrent with the linear extrapolation of the baseline photocurrent was performed. A slight difference is noted in the values, indicating that the $Sb_2Se_3/Pt(PED)$ film promotes an energy reduction of 36 mV for the effective HER initiation. This means that in addition to providing an increase in photocurrent density, the Pt deposited by the PED method results in a decreased overpotential for hydrogen production. However, this value is still far from those found in multilayer systems, which reached ~0.3 V_{RHE} for $Sb_2Se_3/TiO_2/C_{60}/Pt$ [49], and FTO/Au/Bilayer $Sb_2Se_3/TiO_2/Pt$ [7], and ~0.43 V_{RHE} for $Mo/Sb_2Se_3(Se)/CdS/TiO_2/Pt$ [5].

A chronoamperometry for the modified semiconductors, under 0 V_{RHE} and pulsed light incidence, is presented in Fig. 2c with an inset for the Sb_2Se_3 semiconductor without Pt. In general, under chopped illumination, electron-hole pairs form in the absorber and the constant applied potential minimizes the possibility of instantaneous recombination of those charges. When the light is off, the current drops instantly due to the absence of photoexcited charges. In this case, the photocurrent obtained under the incidence of pulsed light, at 0 V_{RHE}, which is the reduction potential for water splitting, for the catalyst without Pt modification is in the order of -0.025 mA cm^{-2}. It is possible to observe a sharp spike when the light is switched on, however, this high initial photocurrent is not sustained, as it drops to a steady-state forming the characteristic plateau corresponding to the competition between charge extraction and charge recombination in the semiconductor [50]. For the catalysts modified with Pt nanoparticles, the system reached higher photocurrent values, under 0 V_{RHE}, around -1.5 mA cm^{-2} and -0.45 mA cm^{-2} for PED and ED, respectively. Additionally, it is possible to observe a steady state for the Sb_2Se_3/Pt
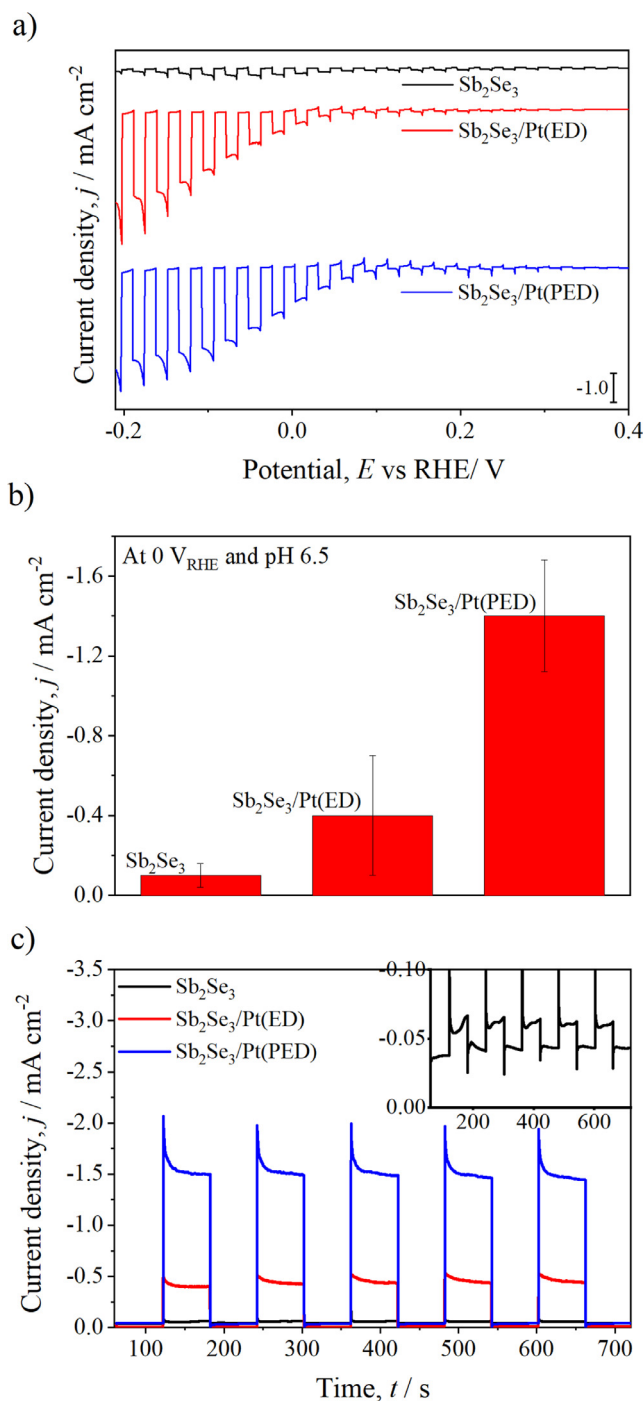

Fig. 2. (a) LSV under pulsed light incidence every 3 s, (b) average value of photocurrent density at 0 V_{RHE}, and (c) chronoamperometry at 0 V_{RHE} with a pulsed light incidence of 60 s for the Sb_2Se_3, $Sb_2Se_3/Pt(ED)$, and $Sb_2Se_3/Pt(PED)$ catalysts.

catalysts compared to the semiconductor without modification, indicating a lower recombination rate between the photogenerated charges. The Sb_2Se_3/Pt catalysts presented a stable photocurrent density along the time of analysis (around 720 s). It is well known that the Sb_2Se_3 semiconductors suffer from photocorrosion in an aqueous medium [35], which brings instability to the catalysts and affects the photocatalytic performance. The Pt in the surface of the semiconductor acts as a charge transfer layer for the catalyst, since the improved charge transfer kinetics in the electrode/electrolyte interface avoids the accumulation of charges that harm the semiconductor.
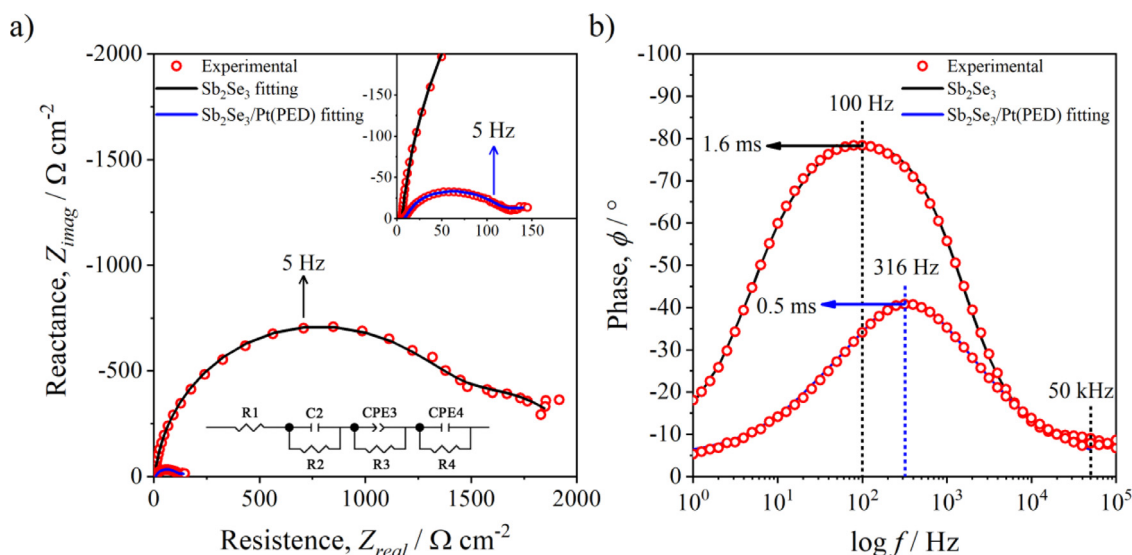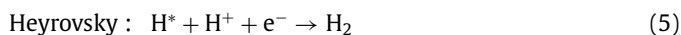
a)

b)

Fig. 3. (a) Nyquist spectra for bare Sb_2Se_3 and Sb_2Se_3/Pt(PED); (b) Bode plots corresponding to the Nyquist spectra, with the symbols representing the experimental data and the solid lines the adjustment based on the equivalent circuit.

It is established that electrocatalysts with elevated activity, such as Pt, Pd, or Ir, are necessary to minimize the overpotential in the HER [51]. The proton reduction occurs with the transfer of two electrons in the presence of intermediate hydrogen (H*) on a site in the electrode surface. The Volmer-Heyrovsky and Volmer-Tafel pathways describe the reaction by the following Eqs. (4) to (6) [52]:

$$Volmer : H^+ + e^- \rightarrow H^* \qquad (4)$$

$$Heyrovsky : H^* + H^+ + e^- \rightarrow H_2 \qquad (5)$$

$$Tafel : 2H^* \rightarrow H_2 + 2^* \qquad (6)$$

The rate of the HER is dependent on the free energy of hydrogen adsorption, ΔG_H. In other words, the hydrogen should not be too weakly or too strongly attached to the site, i.e., ΔG_H must be close to 0 to not be limited by the adsorption (Volmer) or by the desorption (Heyrovsky or Tafel) [53]. It is possible to obtain the volcano curve based on the Sabatier principle from density functional theory (DFT) calculations, where Pt is at the top [54]. It means that Pt features $\Delta G_H \approx 0$ and negligible overpotentials, while semiconductors present several impediments regarding kinetics, such as high recombination rate and slow charge transfer [55]. Proof of that can be observed in the Nyquist curves in the presence and absence of Pt in the Sb_2Se_3 films (Fig. 3a).

The Nyquist plot of Sb_2Se_3/Pt(PED) presented a significant reduction in the resistance to charge transfer compared to the bare Sb_2Se_3 film, which leads to an improvement in the photoelectrocatalytic performance of the catalyst. Impedance measurements were also performed in the dark for this system, however, they provided data that goes beyond the scale of the equipment due to the high resistance to charge transfer in the absence of light, making it impossible to be presented.

The adjustment of the equivalent circuit was performed with the help of the ZView v3.1c software. The errors attributed to each element are below 10% while the Chi-Squared values are below 1×10^{-3} (Fig. S7). The analytical model proposed by Bertoluzzi and Bisquert for solar water splitting was adapted for this system [56]. This model is associated with the different kinetic mechanisms that rule the semiconductor/solution interface for solar wa-

ter splitting, as reported in our previous work [35]. An equivalent circuit composed of three semicircles can be adjusted so that each one of the semicircles corresponds to a resistor-capacitor, which can be connected in series with the electrolyte resistance (the model is in Fig. 3a and all values are described in Table S1). The high-frequency semicircle can be assigned to the charge carriers trapping/de-trapping transfer, while the medium and low-frequency semicircles correspond to the transfer of charge through surface states and via the conduction band, respectively. Fig. 3b presents the Bode graphs with two distinct regions for the Sb_2Se_3 films in the presence and absence of Pt, one of them between 100 and 320 Hz, and the other at 50 kHz. The lower frequency region corresponds to two time constants. From the frequency corresponding to the maximum phase obtained in the peak of the Bode graph, f_{max}, the relaxation time of the electrons is obtained, which indicates the time for the charge to be transferred from the surface of the electrode to the supporting electrolyte, according to the following Eq. (7) [57,58]:

$$\tau_{rel} = \frac{1}{2\pi f_{max}} \qquad (7)$$

The relaxation times (τ_{rel}) calculated for the Sb_2Se_3 film with and without Pt deposition reached 0.5 and 1.6 ms, respectively. It means that the insertion of the cocatalyst in the Sb_2Se_3 film results in faster consumption of the photogenerated electrons and, consequently, in a rapid reduction of protons compared to the bare semiconductor. These results are in agreement with the data obtained by the Nyquist plot and with the decreased resistance to the charge transfer observed for Sb_2Se_3/Pt, reinforcing that the kinetics related to the Sb_2Se_3 film can be strongly improved by the deposition of metallic Pt nanoparticles for the solar water splitting reaction.

3.2. Investigating the PED performance for the Sb_2Se_3/Pt semiconductor compared to ED

To verify if the increase in the photocurrent density of the Sb_2Se_3/Pt semiconductor, concerning the two deposition methods (Fig. 2), can be assigned only to the quantity of Pt nanoparticles deposited on the surface of Sb_2Se_3 (considering that the charge obtained for each case was very different, Fig. 1d and 1e), a deposition of Pt nanoparticles was performed using ED and the same
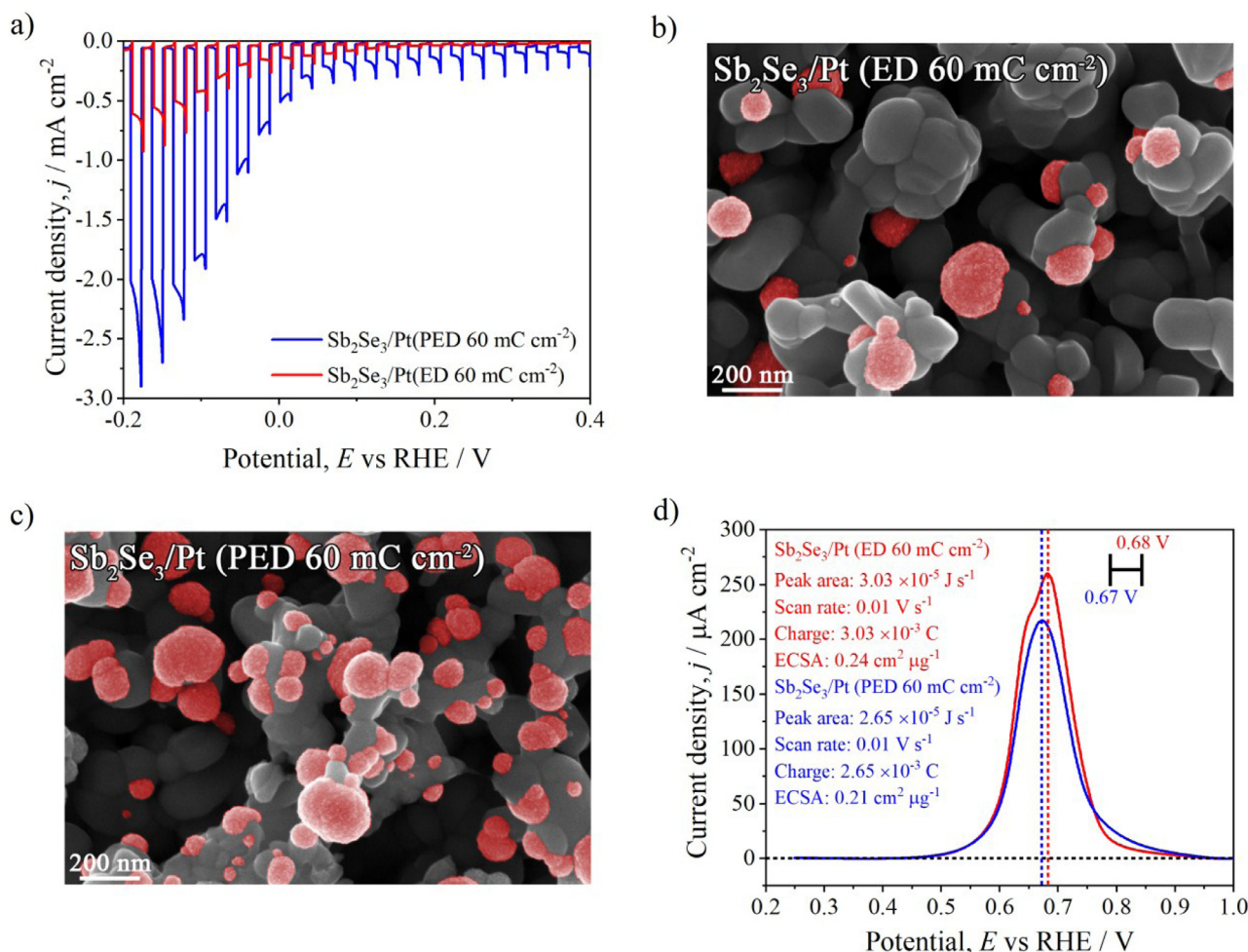
Fig. 4. (a) LSV under pulsed light for the Sb_2Se_3/Pt catalysts prepared by ED and PED fixing 60 mC cm^{-2} for both cases; FEG-SEM images of (b) Sb_2Se_3/Pt(ED) and (c) Sb_2Se_3/Pt(PED); (d) anodic region of the voltammogram for CO oxidation measurements.

charge obtained in the PED method (about 60 mC cm^{-2}). Notice that the deposition of Pt with the same charge for both electrodes indicates that Sb_2Se_3 was modified with the same amount of Pt in both cases (the charge deposition profile for Sb_2Se_3/Pt(ED 60 mC cm^{-2}) is in Fig. S8).

The as-prepared semiconductors were submitted to LSV under pulsed light incidence of 1 sun, as presented in Fig. 4a. Regardless of the fixed charge, a higher photocurrent density is observed, in all potentials analyzed (from 0.4 to −0.2 V$_{RHE}$), for the catalyst prepared using the PED method. As discussed earlier, the presence of light can generate additional sites on the surface of the absorber, which correspond to regions where electron-hole pairs are separated more efficiently. This can be seen from the images of the surfaces of the Sb_2Se_3/Pt(ED) and Sb_2Se_3/Pt(PED) films obtained by SEM (Fig. 4b and 4c, respectively). Although 60 mC cm^{-2} was employed in both depositions, it is possible to notice that on the Sb_2Se_3/Pt(PED) film there are smaller particles better dispersed on the surface (highlighted in red), compared to the Sb_2Se_3/Pt(ED) film. To reinforce this argument, the particles exposed on the surface of the films were counted. With the aid of the Image-J v1.52a software, the areas of visible particles were counted in images with 50k of magnification (Fig. S9a). Due to the low number of particles exposed in the Sb_2Se_3/Pt(ED) film, another image of the same magnification was used to have a more suitable counting. From the Fig. S9b and S9c, it is possible to notice that the Sb_2Se_3/Pt(PED) film presented a greater number of particles with areas of up to

0.045 μm^2, while the Sb_2Se_3/Pt(ED) film was the one that exhibited particles with greater areas, with some reaching ~1 μm^2. This means that under the same deposition charge, the Pt particles that nucleate in the intrinsic sites of the absorber in the absence of light tend to grow their size even more, while in the deposition with the presence of light, more particles with smaller dimensions are distributed on the surface of the film. Hence, the PED of Pt nanoparticles allows a better distribution of Pt on the surface of the semiconductor, improving the photocurrent density, charge transfer, and photoconversion. Consequently, this behavior will positively affect the solar water splitting catalyzed by Sb_2Se_3/Pt(PED).

On the other hand, the deposition of the cocatalyst in the absence of light (ED) possibly occurs in the intrinsic sites of Sb_2Se_3, promoting a low photocurrent density, as can be observed in Fig. 4a. To understand the reason why this phenomenon happens only with the film obtained by the ED method, CO adsorption/oxidation measurements were made on both films and the electrochemical surface area (ECSA) was calculated (Fig. S10a and S10b) [59]. A description of how the analysis was performed is presented in the SI. Considering the ratio between charge and area for the CO monolayer of 420 μC cm^{-2} [60] and the Pt mass of 29.7 μg (from 60 mC cm^{-2} and considering faradaic efficiency of 100%), the ECSA can be obtained (Fig. 4d).

The continuous lines in Fig. S10a and S10b present the first cycle of CO oxidation after the adsorption, which can be at-
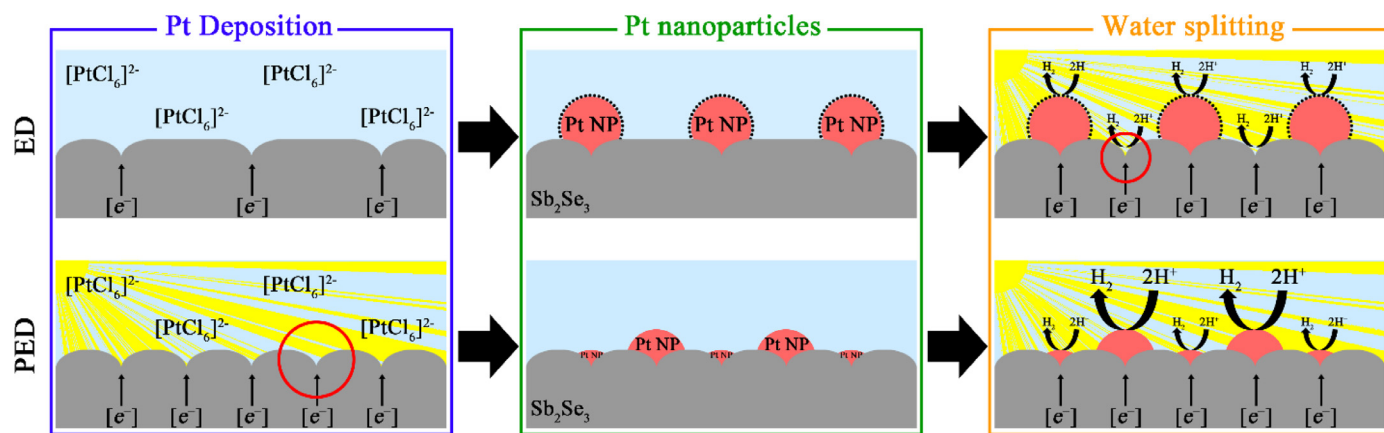
Fig. 5. Proposed scheme summarizing the Pt deposition by PED and ED on Sb_2Se_3 films. The circle in which "Pt" inside represents Pt nanoparticles (Pt NP). The $[e^-]$ symbol represents that there are electrons available for those sites.

tributed to the peaks at 0.68 and 0.67 V_{RHE} for $Sb_2Se_3/Pt(ED)$ and $Sb_2Se_3/Pt(PED)$, respectively. The dashed line (Fig. S10a and S10b) presents the second cycle, where there is the absence of CO in the surfaces of the electrodes and, consequently, the peaks are not observed in both cases. Fig. 4d presents the overlap of both peaks showing a small increment of 14% in the ECSA for the $Sb_2Se_3/Pt(ED)$. Even with a very similar ECSA, the $Sb_2Se_3/Pt(PED)$ catalyst presented a higher photocurrent density, which reinforces the hypothesis of a better distribution of Pt in new active sites using light incidence in the synthesis method. This is also noticed when comparing the roughness factor (R_f) of both films. Considering the electrode area (0.5 cm^2) and CO oxidation charges for $Sb_2Se_3/Pt(ED)$ and $Sb_2Se_3/Pt(PED)$ of 3.03×10^{-3} and 2.65×10^{-3} C, respectively, the R_f values can be obtained by dividing the charge density in both cases (6.06×10^{-3} and 5.30×10^{-3} C cm^{-2}) by the charge required for the oxidation of a CO monolayer from an ideally flat electrode (420 μC cm^{-2}) [61]. The R_f values for the $Sb_2Se_3/Pt(ED)$ and $Sb_2Se_3/Pt(PED)$ films are 14.4 and 12.6, respectively. Despite the same charge being deposited in both films, the absence of photoactivated sites in the $Sb_2Se_3/Pt(ED)$ film contributed to a slight increase in the roughness of the Pt nanoparticles. On the other hand, this change did not significantly affect the photocurrents of the films when normalized by R_f (Fig. S10c), which leads us to believe again that the improvement in the photoactivity of the $Sb_2Se_3/Pt(PED)$ film is due to a better distribution of Pt as result of the photoactivated sites. Additionally, a displacement of 10 mV to less positive potentials can be observed for $Sb_2Se_3/Pt(PED)$, indicating that the bonding strength between Pt and CO in the PED is smaller than the bonding strength obtained by ED and, therefore, the desorption of CO is facilitated in $Sb_2Se_3/Pt(PED)$ [62].

These results have shown that not only there is a different Pt nucleation for the two deposition methods, but also there is a difference in the growth kinetics of the nanoparticles. When establishing a fixed charge, the Pt growth using ED resulted in the agglomeration of Pt, with consequent formation of larger particles, and in the exposure of different faces of the metal to the supporting electrolyte. The crystallographic facets and surface defects such as vacancies, steps, kinks, and terraces can influence the activity of the catalyst [63]. This behavior may have led to the low photocurrent observed in the $Sb_2Se_3/Pt(ED)$ electrode (Fig. 4a). Unfortunately, the small number of Pt nanoparticles deposited over the Sb_2Se_3 catalyst does not allow the identification of facets by X-ray diffraction (XRD).

Concerning the peak in the CV for the $Sb_2Se_3/Pt(ED)$ electrode (Fig. 4d), Feliu and coworkers [64] also observed a shoulder close

to the main peak in the CV for CO oxidation on Pt and associated it with the presence of short terraces in the Pt single crystal. Taylor and coworkers [65] investigated different Pt loadings and observed a profile with multiple peaks in the CV with an increase in the shoulder as the Pt loading increased, suggesting the agglomeration of the metal. Even though the Pt deposited by ED in this study is polycrystalline, it is reasonable to imagine that the presence of superficial defects modifies the shape of the voltammogram, as demonstrated in the literature [64]. This can lead to the shoulder observed at 0.65 V_{RHE} overlaid to the main peak at 0.68 V_{RHE} for the $Sb_2Se_3/Pt(ED)$ film. The absence of this shoulder in the $Sb_2Se_3/Pt(PED)$ film could indicates a better uniformity of the Pt nanoparticle in the deposition assisted by light.

The better uniformity in the Pt nanoparticle deposition is intimately related to the higher number of sites available for the metal deposition, which was observed in the PED method. According to Nakibli and coworkers [66], for multielectron reactions, such as hydrogen evolution and CO_2 reduction, the best design for the photocatalyst includes the distribution of a single cocatalyst per site to ensure proximity of the intermediates that are formed in the multistep reaction, ideally allowing all of them to be formed on the same catalytic site. This reinforces the reasoning for the better performance of the catalysts synthesized under PED.

Fig. 5 summarizes the possible differences between the Pt deposition mechanisms discussed thus far for the PED and ED methods. In the PED of Pt, new sites are formed on the surface of Sb_2Se_3 (highlighted in the red circle) due to the incidence of photons, generating more electrons and, consequently, more charge for the Pt reduction, while the ED of Pt is characterized by the formation of vacancies, steps, kinks, and terraces (dotted contour). As a result, the distribution of Pt nanoparticles in the surface of the semiconductor is different for each case, culminating in solar water splitting favored by the light-assisted Pt deposition method.

3.3. Evaluation of the time in the synthesis of Sb_2Se_3/Pt by PED

The data presented above proved that the PED method is more efficient than the ED method to deposit Pt nanoparticles seeking a photocatalyst with greater photocurrent density and fast synthesis method. On the other hand, it is well known that there is a necessity to optimize the catalyst synthesis to obtain the best photoactivity possible from the material [23,35], especially considering the economic aspect related to the deposition of noble metals and scalability. Therefore, different times (1, 5, 10, and 15 min) of Pt deposition by PED on the Sb_2Se_3 surface were investigated and

the results concerning the physical, chemical, and photochemical characterizations are presented ahead.

FEG-SEM images of the catalysts prepared within different times of PED are presented in Fig. 6. It is easy to conclude that there is a tendency in the deposition; as expected, the longer PED takes, the greater the Pt coverage on the surface of the semiconductor. For the film prepared with 1 min of PED (Fig. 6a), the deposition of the metal occurs especially in the most external area of the Sb_2Se_3 agglomerates. Increasing the time of PED, the deposition of Pt starts to occur in more internal regions of the Sb_2Se_3, as can be observed in Fig. 6b (5 min of deposition). Massive coverage of the substrate surface starts after 10 min of Pt deposition (Fig. 6c), therefore, at 15 min of PED it is not possible to observe any surface of Sb_2Se_3 exposed (Fig. 6d). Even with a similar distribution of Pt nanoparticles in the catalyst with 10 and 15 min of PED, the quantities deposited in both cases are completely different, as indicated by the average charge obtained for each case, presented in Fig. S11. The charge obtained for the catalysts prepared with 15 min of PED is twice the charge observed for the catalyst synthesized with 10 min of PED, showing that Pt deposition is an autocatalytic process.
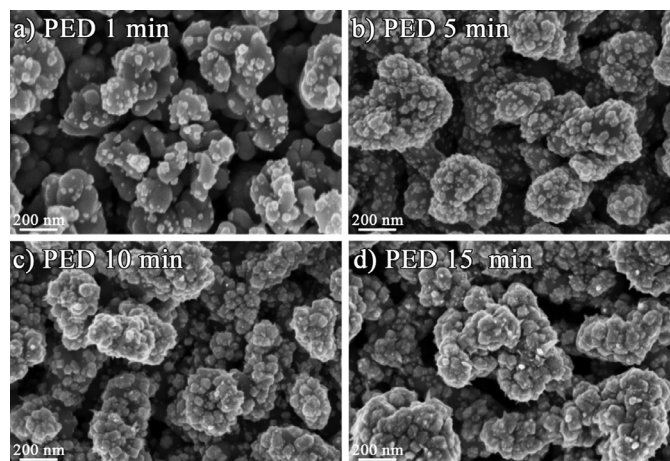
Fig. 6. FEG-SEM images obtained with 150 k of magnification for the surface of Sb_2Se_3/Pt catalysts synthesized with (a) 1 min, (b) 5 min, (c) 10 min, and (d) 15 min of PED.
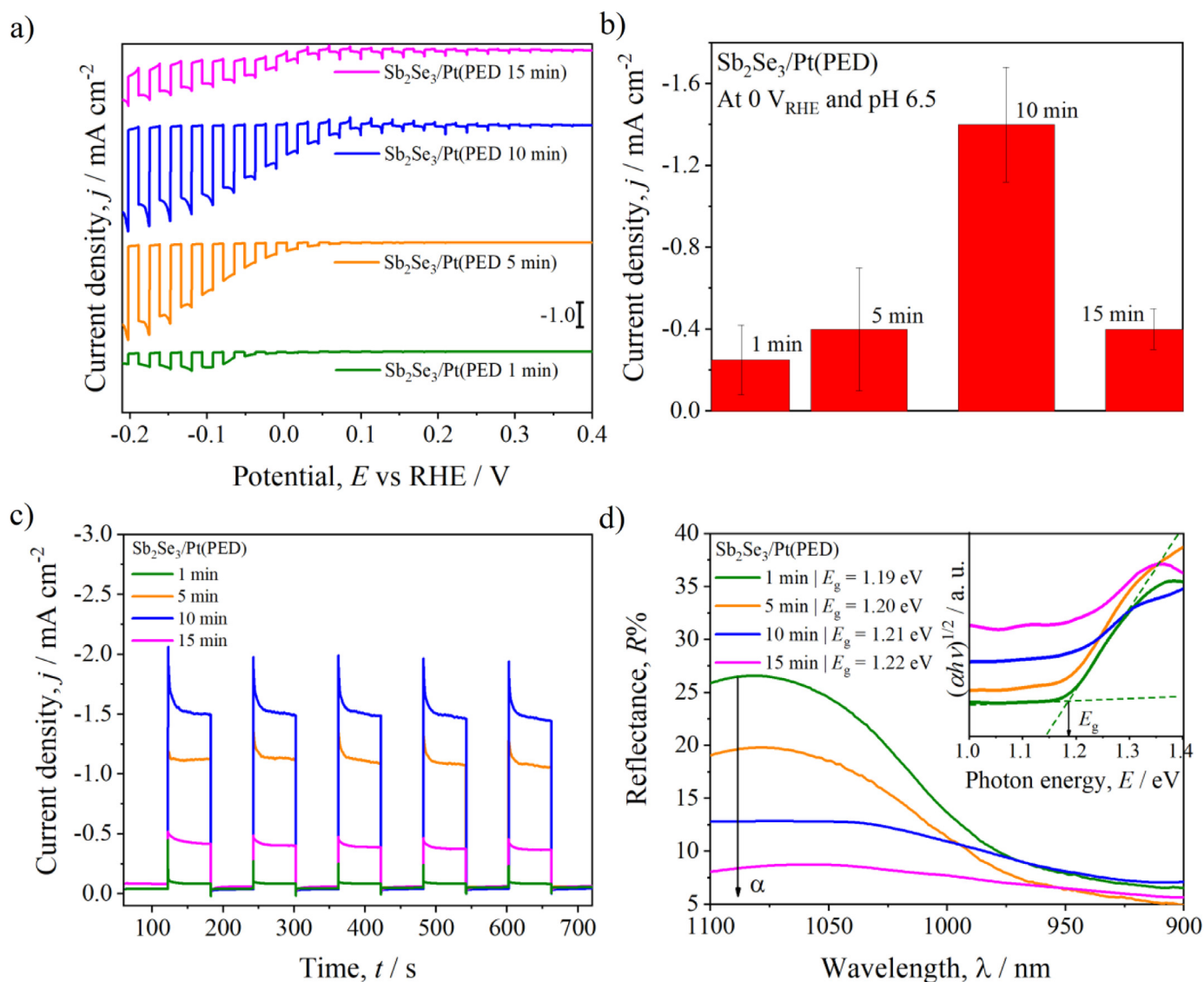
Fig. 7. (a) LSV under pulsed light incidence, (b) average value of photocurrent density at 0 V_{RHE}, (c) chronoamperometry under pulsed light incidence at 0 V_{RHE} for the Sb_2Se_3/Pt(PED) catalysts prepared with 1, 5, 10, and 15 min of deposition, and (d) diffuse reflectance spectra with inserted Tauc's plot.

Table 1

Kinetics parameters of Sb_2Se_3 semiconductor modified with Pt nanoparticles by PED using different times of deposition.

|	τ / s	η_{trans}	k_{trans} / s^{-1}	k_{rec} / s^{-1}
PED 1 min	8.33 ± 0.13	0.69 ± 0.01	0.08 ± 0.01	0.037 ± 0.001
PED 5 min	5.75 ± 0.12	0.83 ± 0.01	0.12 ± 0.04	0.024 ±0.008
PED 10 min	7.51 ± 0.75	0.77 ± 0.01	0.10 ± 0.01	0.031 ± 0.003
PED 15 min	8.50 ± 0.25	0.81 ± 0.01	0.10 ± 0.01	0.022 ± 0.001

Exposition of the Sb_2Se_3 film is extremely important for the photoactivity of the material since the semiconductor needs to be accessible to the incident photons to photogenerate the electron-hole pairs; it is only after this step that the Pt nanoparticles can contribute to the charge separation by scavenging the electrons from the conduction band (CB). This is confirmed by the photocurrent curves presented in Fig. 7a for each different deposition time. The average value of the photocurrent obtained at 0 V_{RHE} from the replicates is presented in Fig. 7b for each as-prepared material. The catalyst prepared with 15 min of PED presented low values of photocurrent density (−0.4 ±0.1 mA cm^{-2}). The extremely high amount of Pt covering the Sb_2Se_3 surface blocked the light from reaching the semiconductor, making it impossible for the semiconductor to be photoactivated. Similarly, the catalyst prepared with 1 min of PED presented a photocurrent density below −0.25 ±0.17 mA cm^{-2}, due to the small number of Pt nanoparticles, which culminated in the low possibility of transferring photogenerated electrons to the metal. The best condition was observed for the catalyst prepared with 10 min of PED, which presented the highest photocurrent density value, −1.4 ±0.3 mA cm^{-2}. It is worth mentioning that, at a potential 100 mV more negative than the thermodynamic potential related to the reduction of protons, the photocurrent density for the catalyst Sb_2Se_3/Pt(PED 10 min) reached approximately −3.0 mA cm^{-2}, which is very expressive for a catalyst composed just of a semiconductor and a cocatalyst activated by 1 sun of light incidence.

Fig. 7c shows the transient photocurrent for all catalysts presenting a stable photocurrent density along the time of the pulses in all cases, with reproductive behavior of decay, indicating that there was no change in the charge recombination kinetics along the time of irradiation or with the time of Pt deposition by PED [67]. To confirm that the Pt nanoparticles are acting as a barrier layer on the Sb_2Se_3 semiconductor, an investigation was performed concerning the change in the kinetic rate constant of the films by analysis of the decay profile for the three last pulses of the transient photocurrent from Fig. 7c. Details of the analysis for the different Pt deposition times can be seen in Fig. S12. The time-constant transient (τ) can be calculated by Eq. (8) [68,69]:

$$\frac{j_t - j_{ss}}{j_{in} - j_{ss}} = D = e^{-t/\tau} \tag{8}$$

where j_t is the photocurrent density in a specific interval time t, j_{ss} is the photocurrent density in the steady-state, and j_{in} is the photocurrent density at the beginning of the decay. Furthermore, the kinetic rate constants of electron transfer and electron recombination (k_{trans} and k_{rec}, respectively) and the efficiency in the electron transfer (η_{trans}) can be obtained by Eq. (9) [70]:

$$\eta_{trans} = \frac{j_{ss}}{j_{in}} = \frac{k_{trans}}{k_{trans} + k_{rec}} \tag{9}$$

Considering that the decay of the photocurrent transient is a rate law of first or pseudo-first-order reaction, a constant of transient time obeys $\tau = (k_{trans} + k_{rec})^{-1}$ [70,71]. The values of kinetic constants did not present a significant change among the catalysts synthesized under different times of PED, as presented in Table 1.

This means that the quantity of Pt deposited by PED did not significantly influence the kinetic parameters and the charge recombination, considering a saturation level reached with 5 min of PED. It helps to support the conclusion that the decrease in the photocurrent density for the catalyst prepared with 15 min of PED is associated only with the decrease of the probability of photons reaching the surface of the semiconductor.

The formation of a blocking Pt layer on the Sb_2Se_3 surface can also be inferred from the behavior observed in the diffuse reflectance analysis and the increase in α according to the increase in the Pt loading shown in Fig. 7d. The presence of Pt in the catalyst promoted lower values of reflectance in the near-infrared region due to the surface plasmon resonance phenomenon, as observed in Fig. S5a. This phenomenon is also observed under different times of Pt deposition, however, in this case, the intensity of the effect is more pronounced for longer times of PED. This behavior caused a range in the reflectance between ~7.5 and 25 %, moreover, it is accompanied by the increase of the α in lower energy regions. The catalysts synthesized with different times of PED did not present a substantial difference in the E_g values, since Sb_2Se_3 is the only component that presents a bandgap energy, implying that the absorption observed in Fig. 8d is related to the presence of Pt and its surface plasmon resonance effect.

4. Conclusion

This study presents the analysis of two different methods for the deposition of Pt on the Sb_2Se_3 semiconductor. The electrodeposition method is commonly employed for the synthesis of Pt nanoparticles in the literature; however, the resulting material presented much poorer performance compared to the catalyst obtained from electrodeposition assisted by light incidence (photoelectrodeposition). The Sb_2Se_3/Pt catalysts prepared by PED presented a greater number of Pt nanoparticles well dispersed on the semiconductor surface under a shorter time of deposition and with a photocurrent density over three times higher compared to the catalysts prepared by ED under the same conditions. The better achievements from PED are probably related to the increase in the number of available sites for the deposition of the noble metal due to the activation of the semiconductor by the incidence of photons. Additionally, the optimization of the conditions of the synthesis using PED was investigated, reaching a material that presented −1.4 ± 0.3 mA cm^{-2} of photocurrent density at 0 V_{RHE}, a value more than 10 times higher than the photocurrent density obtained for the semiconductor without modification.

Declaration of Competing Interest

The authors declare that they have no known competing financial interests or personal relationships that could have appeared to influence the work reported in this paper.

Credit authorship contribution statement

Marcos Vinicius de Lima Tinoco: Investigation, Methodology, Data curation, Writing - original draft, Writing - review & editing. **Magno Barcelos Costa:** Investigation, Methodology, Data curation, Writing - original draft, Writing - review & editing. **Lucia Helena Mascaro:** Visualization, Writing - review & editing, Resources. **Juliana Ferreira de Brito:** Visualization, Supervision, Writing - review & editing, Resources.

Supplementary materials

Supplementary material associated with this article can be found, in the online version, at doi:10.1016/j.electacta.2021.138290.

References

[1] M.B. Costa, F.W. de Souza Lucas, L.H. Mascaro, Thermal treatment effects on electrodeposited Sb$_2$Se$_3$ photovoltaic thin films, ChemElectroChem 4 (2017) 2507–2514.

[2] G. Centi, S. Perathoner, Towards solar fuels from water and CO$_2$, ChemSusChem 3 (2010) 195–208.

[3] Y. Zhao, G.I.N. Waterhouse, G. Chen, X. Xiong, L.-Z. Wu, C.-H. Tung, T. Zhang, Two-dimensional-related catalytic materials for solar-driven conversion of COx into valuable chemical feedstocks, Chem. Soc. Rev. 48 (2019) 1972–2010.

[s4] J.F.d. Brito, P.G. Corradini, M.V.B. Zanoni, F. Marken, L.H. Mascaro, The influence of metallic Bi in BiVO4 semiconductor for artificial photosynthesis, J. Alloys Compd. 851 (2021).

[5] L. Zhang, Y. Li, C. Li, Q. Chen, Z. Zhen, X. Jiang, M. Zhong, F. Zhang, H. Zhu, Scalable low-band-gap Sb$_2$Se$_3$ thin-film photocathodes for efficient visible–near-infrared solar hydrogen evolution, ACS Nano 11 (2017) 12753–12763.

[6] W. Yang, J.H. Kim, O.S. Hutter, L.J. Phillips, J. Tan, J. Park, H. Lee, J.D. Major, J.S. Lee, J. Moon, Benchmark performance of low-cost Sb$_2$Se$_3$ photocathodes for unassisted solar overall water splitting, Nat. Commun. 11 (2020) 861.

[7] J. Park, W. Yang, J. Tan, H. Lee, J.W. Yun, S.G. Shim, Y.S. Park, J. Moon, Hierarchal nanorod-derived bilayer strategy to enhance the photocurrent density of Sb$_2$Se$_3$ photocathodes for photoelectrochemical water splitting, ACS Energy Lett 5 (2020) 136–145.

[8] J. Park, W. Yang, Y. Oh, J. Tan, H. Lee, R. Boppella, J. Moon, Efficient solar–to-hydrogen conversion from neutral electrolytes using morphology-controlled Sb$_2$Se$_3$ light absorbers, ACS Energy Lett. 4 (2019) 517–526.

[9] H. Wang, J.L. Faria, S. Dong, Y. Chang, Mesoporous Au/TiO$_2$ composites preparation, characterization, and photocatalytic properties, Mater. Sci. Eng. B 177 (2012) 913–919.

[10] D. Sedaries, C. Levy-Clement, C. Godart, Photoelectrodeposition of Nobel metal Islands onto p-InSe, ChemInform 21 (1990) 1733–1739.

[11] D.W. Redman, H.J. Kim, K.J. Stevenson, M.J. Rose, Photo-assisted electrodeposition of MoSx from ionic liquids on organic-functionalized silicon photoelectrodes for H$_2$ generation, J. Mater. Chem. A. 4 (2016) 7027–7035.

[12] Z. Jiang, Z. Zhang, W. Shangguan, M.A. Isaacs, L.J. Durndell, C.M.A. Parlett, A.F. Lee, Photodeposition as a facile route to tunable Pt photocatalysts for hydrogen production: on the role of methanol, Catal. Sci. Technol. 6 (2016) 81–88.

[13] E.M.P. Steinmiller, K.-S. Choi, Photochemical deposition of cobalt-based oxygen evolving catalyst on a semiconductor photoanode for solar oxygen production, Proc. Natl. Acad. Sci. 106 (2009) 20633–20636.

[14] Y.L. Kawamura, T. Sakka, Y.H. Ogata, Photoassisted control of Pt Electrodeposition on p-Type Si, J. Electrochem. Soc. 152 (2005) C701.

[15] D.K. Zhong, J. Cornuz, K. Sivula, M. Grätzel, D.R. Gamelin, Photo-assisted electrodeposition of cobalt–phosphate (Co–Pi) catalyst on hematite photoanodes for solar water oxidation, Energy Environ. Sci. 4 (2011) 1759.

[16] R. Shoji, Y. Mochizuki, Y. Kobayashi, N. Yamauchi, K. Sato, Adsorption and photoelectrodeposition of heavy metal ions, Glob. J. Res. Eng. C Chem. Eng. 18 (2018) 23–35.

[17] T. Chang, W. Lee, Y. Su, Y. Hsiao, Effects of photo-assisted electrodeposited on CuInSe2 thin films, Nanoscale Res. Lett. 9 (2014) 660.

[18] Y.L. Kawamura, T. Sakka, Y.H. Ogata, Influence of Illumination on morphology of metal electrodeposits on p-type Si, Electrochemistry 76 (2008) 121–124.

[19] T.T. Guaraldo, J.F. Brito, D. Wood, M.V.B. Zanoni, A New Si/TiO2/Pt p-n junction semiconductor to demonstrate photoelectrochemical CO$_2$ conversion, Electrochim. Acta. 185 (2015) 117–124.

[20] C. Genovese, C. Ampelli, S. Perathoner, G. Centi, A gas-phase electrochemical reactor for carbon dioxide reduction back to liquid fuels, Chem. Eng. Trans. 32 (2013) 289–294.

[21] V. Subramanian, E. Wolf, P.V. Kamat, Semiconductor-metal composite nanostructures. To what extent do metal nanoparticles improve the photocatalytic activity of TiO$_2$ films? J. Phys. Chem. B 105 (2001) 11439–11446.

[22] W. Septina, S. Ikeda, T. Harada, M. Higashi, R. Abe, Photosplitting of water from wide-gap Cu (In, Ga)S2 thin films modified with a CdS Layer and Pt nanoparticles for a high-onset- potential photocathode, J. Phys. Chem. C. 119 (2015) 8576–8583.

[23] M. Medina, P. Corradini, L.H. Mascaro, Facile one-step electrodeposition fabrication of amorphous MoS$_2$ catalysts in titanium for hydrogen evolution reaction, J. Braz. Chem. Soc. 00 (2019) 1–9.

[24] Y.F. Tay, H. Kaneko, S.Y. Chiam, S. Lie, Q. Zheng, B. Wu, S.S. Hadke, Z. Su, P.S. Bassi, D. Bishop, T.C. Sum, T. Minegishi, J. Barber, K. Domen, L.H. Wong, Solution-Processed Cd-Substituted CZTS photocathode for efficient solar hydrogen evolution from neutral water, Joule 2 (2018) 537–548.

[25] W. Yang, J. Moon, Rapid advances in antimony triselenide photocathodes for solar hydrogen generation, J. Mater. Chem. A. 7 (2019) 20467–20477.

[26] C. Chen, W. Li, Y. Zhou, C. Chen, M. Luo, X. Liu, K. Zeng, B. Yang, C. Zhang, J. Han, J. Tang, Optical properties of amorphous and polycrystalline Sb$_2$Se$_3$ thin films prepared by thermal evaporation, Appl. Phys. Lett. 107 (2015) 043905.

[27] Y. Zhou, L. Wang, S. Chen, S. Qin, X. Liu, J. Chen, D.-J. Xue, M. Luo, Y. Cao, Y. Cheng, E.H. Sargent, J. Tang, Thin-film Sb$_2$Se$_3$ photovoltaics with oriented one-dimensional ribbons and benign grain boundaries, Nat. Photonics. 9 (2015) 409–415.

[28] Y. Zhou, M. Leng, Z. Xia, J. Zhong, H. Song, X. Liu, B. Yang, J. Zhang, J. Chen, K. Zhou, J. Han, Y. Cheng, J. Tang, Solution-processed antimony selenide heterojunction solar cells, Adv. Energy Mater. 4 (2014) 1301846.

[29] X. Liu, J. Chen, M. Luo, M. Leng, Z. Xia, Y. Zhou, S. Qin, D. Xue, L. Lv, H. Huang, D. Niu, J. Tang, Thermal evaporation and characterization of Sb$_2$Se$_3$ thin film for substrate Sb$_2$Se$_3$/CdS solar cells, ACS Appl. Mater. Interfaces 6 (2014) 10687–10695.

[30] M.B. Costa, F.W. de Souza Lucas, L.H. Mascaro, Electrodeposition of Fe-doped Sb$_2$Se$_3$ thin films for photoelectrochemical applications and study of the doping effects on their properties, J. Solid State Electrochem. 22 (2018) 1557–1562.

[31] K. Zeng, D.-J. Xue, J. Tang, Antimony selenide thin-film solar cells, Semicond. Sci. Technol. 31 (2016) 1–13.

[32] K.-Y. Lee, K. Sato, A.R. Mohamed, Facile synthesis of anatase-rutile TiO$_2$ composites with enhanced CO$_2$ photoreduction activity and the effect of Pt loading on product selectivity, Mater. Lett. 163 (2016) 240–243.

[33] L.C. Almeida, M.V.B. Zanoni, Decoration of Ti/TiO$_2$ nanotubes with Pt nanoparticles for enhanced UV-Vis light absorption in photoelectrocatalytic process, J. Braz. Chem. Soc. (2014).

[34] W. Septina, S.Ikeda Gunawan, T. Harada, M. Higashi, R. Abe, M. Matsumura, Photosplitting of water from wide-gap Cu(In,Ga)S2 thin films modified with a CdS layer and Pt nanoparticles for a high-onset-potential photocathode, J. Phys. Chem. C. 119 (2015) 8576–8583.

[35] M.B. Costa, F.W. de S. Lucas, M. Medina, L.H. Mascaro, All-electrochemically–grown Sb$_2$Se$_3$/a-MoSx photocathode for hydrogen production: the effect of the MOSX layer on the surface recombination and photocorrosion of Sb$_2$Se$_3$ Films, ACS Appl. Energy Mater. (2020) acsaem.0c01413.

[36] M. Nowak, B. Kauch, P. Szperlich, Determination of energy band gap of nanocrystalline SbSI using diffuse reflectance spectroscopy, Rev. Sci. Instrum. 80 (2009) 046107.

[37] L. Wang, C. Lee, P. Schmuki, Solar water splitting: preserving the beneficial small feature size in porous a-Fe$_2$O$_3$ photoelectrodes during annealing, J. Mater. Chem. A. 1 (2013) 212–215.

[38] M.B. Costa, F.W.S. Lucas, L.H. Mascaro, Electrodeposition conditions effect Sb$_2$Se$_3$ thin-film properties, ChemElectroChem 6 (2019) 2937–2944.

[39] X. Tao, W. Shi, B. Zeng, Y. Zhao, N. Ta, S. Wang, A.A. Adenle, R. Li, C. Li, Photoinduced surface activation of semiconductor photocatalysts under reaction conditions: a commonly overlooked phenomenon in photocatalysis, ACS Catal. 10 (2020) 5941–5948.

[40] J.A. Seabold, K.-S. Choi, Efficient and stable photo-oxidation of water by a bismuth vanadate photoanode coupled with an iron oxyhydroxide oxygen evolution catalyst, J. Am. Chem. Soc. 134 (2012) 2186–2192.

[41] D. Grujicic, B. Pesic, Electrodeposition of copper: the nucleation mechanisms, Electrochim. Acta. 47 (2002) 2901–2912.

[42] F. Pastorek, B. Hadzima, M. Omasta, M. Mhaede, Effect of electrodeposition temperature on corrosion resistance of calcium phosphate, Acta Metall. Slovaca 20 (2014) 200–208.

[43] A. Shongalova, M.R. Correia, B. Vermang, J.M.V. Cunha, P.M.P. Salomé, P.A. Fernandes, On the identification of Sb$_2$Se$_3$ using Raman scattering, MRS Commun. 8 (2018) 1–6.

[44] N.B. Singh, U. Sarkar, Structure, vibrational, and optical properties of platinum cluster: a density functional theory approach, J. Mol. Model. 20 (2014) 2537.

[45] M.B. Costa, F.W.S. Lucas, L.H. Mascaro, Improvement of electrodeposited Sb$_2$Se$_3$ thin film photoelectroactivity by cobalt grain boundary modification, J. Mater. Chem. A (2020).

[46] A. Li, L. Long, F. Liu, J. Liu, X. Wu, Y. Ji, Antigen-labeled mesoporous silica–coated Au-core Pt-shell nanostructure: a novel nanoprobe for highly efficient virus diagnosis, J. Biol. Eng. 13 (2019) 87.

[47] R. Vadapoo, S. Krishnan, H. Yilmaz, C. Marin, I. Antimony, Electronic structure of antimony selenide (Sb$_2$Se$_3$) from GW calculations, Phys. Status Solidi B 248 (2011) 700–705.

[48] A. Mavlonov, T. Razykov, F. Raziq, J. Gan, J. Chantana, Y. Kawano, T. Nishimura, H. Wei, A. Zakutayev, T. Minemoto, X. Zu, S. Li, L. Qiao, A review of Sb_2Se_3 photovoltaic absorber materials and thin-film solar cells, Sol. Energy 201 (2020) 227–246.

[49] J. Tan, W. Yang, Y. Oh, H. Lee, J. Park, R. Boppella, J. Kim, J. Moon, Fullerene as a photoelectron transfer promoter enabling stable TiO_2-Protected Sb_2Se_3 photocathodes for photo-electrochemical water splitting, Adv. Energy Mater. 9 (2019) 1900179.

[50] M. Mokhtarimehr, S.A. Tatarkova, Photocurrent transients of thin-film solar cells, J. Opt. Soc. Am. B. 34 (2017) 1705.

[51] Y. Jiao, Y. Zheng, M. Jaroniec, S.Z. Qiao, Design of electrocatalysts for oxygen- and hydrogen-involving energy conversion reactions, Chem. Soc. Rev. 44 (2015) 2060–2086.

[52] E. Skúlason, V. Tripkovic, M.E. Björketun, S. Gudmundsdóttir, G. Karlberg, J. Rossmeisl, T. Bligaard, H. Jónsson, J.K. Nørskov, Modeling the electrochemical hydrogen oxidation and evolution reactions on the basis of density functional theory calculations, J. Phys. Chem. C 114 (2010) 18182–18197.

[53] Z.W. Seh, J. Kibsgaard, C.F. Dickens, I. Chorkendorff, J.K. Nørskov, T.F. Jaramillo, Combining theory and experiment in electrocatalysis: insights into materials design, Science 355 (2017) eaad4998.

[54] W. Luo, J. Gan, Z. Huang, W. Chen, G. Qian, X. Zhou, X. Duan, Boosting HER performance of Pt-based catalysts immobilized on functionalized vulcan carbon by atomic layer deposition, Front. Mater. 6 (2019).

[55] T.A. Pham, Y. Ping, G. Galli, Modelling heterogeneous interfaces for solar water splitting, Nat. Mater. 16 (2017) 401–408.

[56] L. Bertoluzzi, J. Bisquert, Equivalent circuit of electrons and holes in thin semiconductor films for photoelectrochemical water splitting applications, J. Phys. Chem. Lett. 3 (2012) 2517–2522.

[57] Y. Yang, X. Zhong, K. Liu, J. Du, Y. Yang, H. He, Y. Zhou, F. Dong, C. Fu, J. Wang, Insight into the improvement mechanism of copper $Oxide/BiVO_4$ heterojunction photoanodes for solar water oxidation, J. Electrochem. Soc. 166 (2019) H513–H520.

[58] X.-C. Dai, M.-H. Huang, Y.-B. Li, T. Li, B.-B. Zhang, Y. He, G. Xiao, F.-X. Xiao, Regulating spatial charge transfer over intrinsically ultrathin-carbon-encapsulated photoanodes toward solar water splitting, J. Mater. Chem. A 7 (2019) 2741–2753.

[59] T. Binninger, E. Fabbri, R. Kötz, T.J. Schmidt, Determination of the electrochemically active surface area of metal-oxide supported platinum catalyst, J. Electrochem. Soc. 161 (2014) H121–H128.

[60] S.-S. Li, Y.-Y. Hu, J.-J. Feng, Z.-Y. Lv, J.-R. Chen, A.-J. Wang, Rapid room-temperature synthesis of Pd nanodendrites on reduced graphene oxide for catalytic oxidation of ethylene glycol and glycerol, Int. J. Hydrogen Energy 39 (2014) 3730–3738.

[61] D. Chen, Q. Tao, L.W. Liao, S.X. Liu, Y.X. Chen, S. Ye, Determining the active surface area for various platinum electrodes, Electrocatalysis 2 (2011) 207–219.

[62] D. Schonvogel, J. Hülstede, P. Wagner, I. Kruusenberg, K. Tammeveski, A. Dyck, C. Agert, M. Wark, Stability of Pt nanoparticles on alternative carbon supports for oxygen reduction reaction, J. Electrochem. Soc. 164 (2017) F995–F1004.

[63] E.G. Ciapina, S.F. Santos, E.R. Gonzalez, Electrochemical CO stripping on nano-sized Pt surfaces in acid media: a review on the issue of peak multiplicity, J. Electroanal. Chem. 815 (2018) 47–60.

[64] F.J. Vidal-Iglesias, J. Solla-Gullón, J.M. Campiña, E. Herrero, A. Aldaz, J.M. Feliu, CO monolayer oxidation on stepped Pt(S) [(n−1)(100)×(110)] surfaces, Electrochim. Acta 54 (2009) 4459–4466.

[65] S. Taylor, E. Fabbri, P. Levecque, T.J. Schmidt, O. Conrad, The effect of platinum loading and surface morphology on oxygen reduction activity, Electrocatalysis 7 (2016) 287–296.

[66] Y. Nakibli, P. Kalisman, L. Amirav, Less is more: The case of metal cocatalysts, J. Phys. Chem. Lett. 6 (2015) 2265–2268.

[67] L.M. Peter, Dynamic aspects of semiconductor photoelectrochemistry, Chem. Rev. 90 (1990) 753–769.

[68] R. Dholam, N. Patel, A. Santini, A. Miotello, Efficient indium tin oxide/Cr-doped-TiO_2 multilayer thin films for H_2 production by photocatalytic water-splitting, Int. J. Hydrogen Energy 35 (2010) 9581–9590.

[69] F. Spadavecchia, S. Ardizzone, G. Cappelletti, L. Falciola, M. Ceotto, D. Lotti, Investigation and optimization of photocurrent transient measurements on nano-TiO2, J. Appl. Electrochem. 43 (2013) 217–225.

[70] M. Rohloff, S. Cosgun, C. Massué, T. Lunkenbein, A. Senyshyn, M. Lerch, A. Fischer, M. Behrens, The role of synthesis conditions for structural defects and lattice strain in β-TaON and their effect on photo- and photoelectrocatalysis, Zeitschrift Für Naturforsch. B. 74 (2019) 71–83.

[71] L.M. Peter, Energetics and kinetics of light-driven oxygen evolution at semiconductor electrodes: the example of hematite, J. Solid State Electrochem. 17 (2013) 315–326.